Lawrence Berkeley National Laboratory
LBL Publications

Title
2D MXenes: A New Family of Promising Catalysts for the Hydrogen Evolution Reaction

Permalink
https://escholarship.org/uc/item/4p334998

Journal
ACS Catalysis, 7(1)

ISSN
2155-5435

Authors
Gao, Guoping
O'Mullane, Anthony P
Du, Aijun

Publication Date
2017-01-06

DOI
10.1021/acscatal.6b02754

Peer reviewed

eScholarship.org Powered by the California Digital Library
University of California

ACS Catalysis

JANUARY 2017 VOLUME 7 NUMBER 1 PUBS.ACS.ORG/ACSCATALYSIS

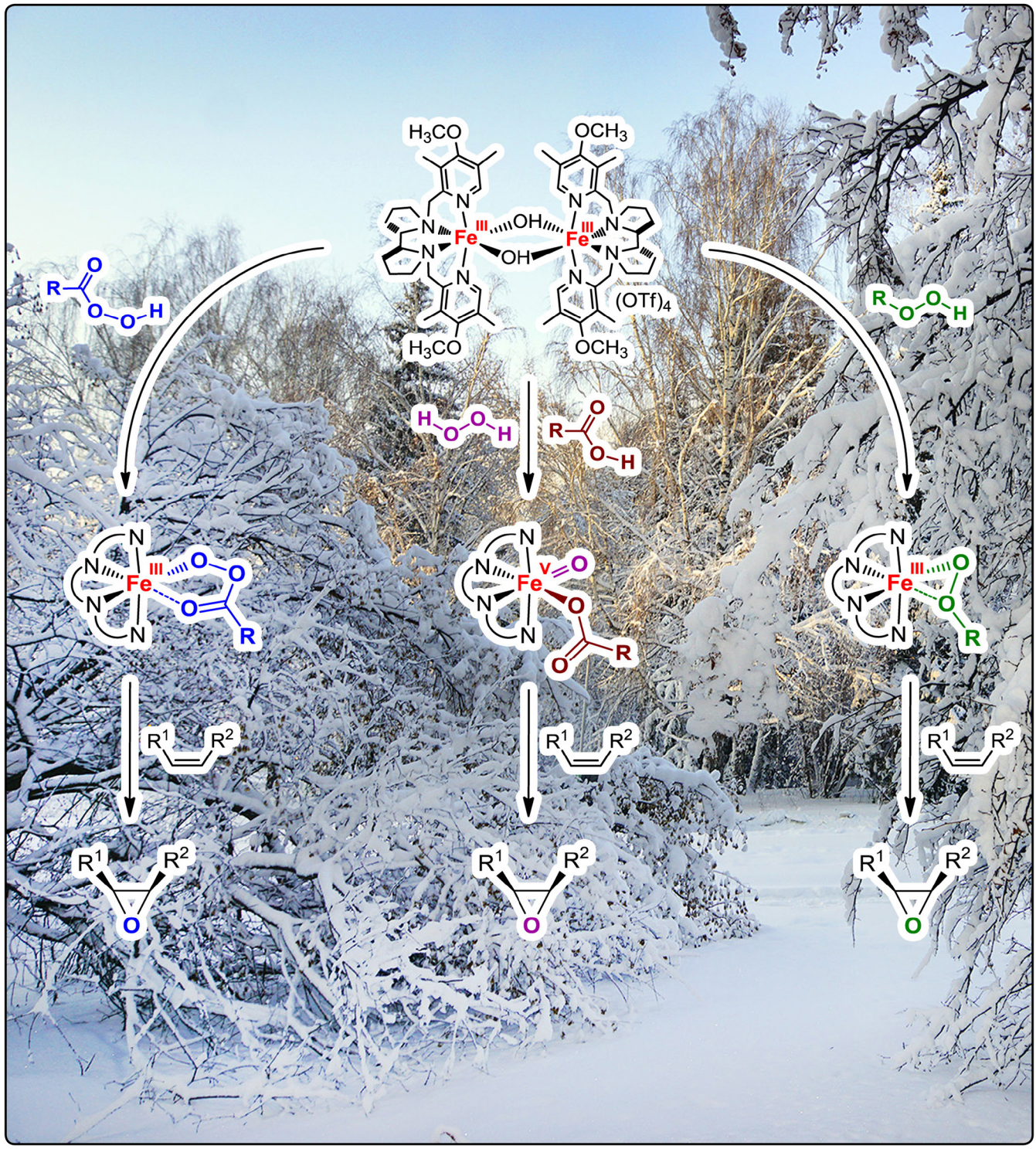

ACS Publications
Most Trusted. Most Cited. Most Read.

www.acs.org

ACS Catalysis

Research Article

pubs.acs.org/acscatalysis

2D MXenes: A New Family of Promising Catalysts for the Hydrogen Evolution Reaction

Guoping Gao, Anthony P. O'Mullane, and Aijun Du*

School of Chemistry, Physics and Mechanical Engineering, Science and Engineering Faculty, Queensland University of Technology (QUT), Gardens Point Campus, Brisbane, QLD 4001, Australia

Supporting Information

ABSTRACT: Developing highly conductive, stable, and active nonprecious hydrogen evolution reaction (HER) catalysts is a key step for the proposed hydrogen economy. However, few catalysts, except for noble metals, meet all the requirements. By using state-of-the-art density functional calculations, herein we demonstrate that 2D MXenes, like Ti_2C, V_2C, and Ti_3C_2, are terminated by a mixture of oxygen atoms and hydroxyl, while Nb_2C and $Nb_4C_3O_2$ are fully terminated by oxygen atoms under standard conditions [pH 0, $p(H_2)$ = 1 bar, U = 0 V vs standard hydrogen electrode], findings in good agreement with experimental observation. Furthermore, all these MXenes are conductive under standard conditions, thus allowing high charge transfer kinetics during the HER. Remarkably, the Gibbs free energy for the adsorption of atomic hydrogen ($\Delta G^0_{H^*}$) on the terminated O atoms (e.g., Ti_2CO_2) is close to the ideal value (0 eV). Our results demonstrate terminated oxygens as catalytic active sites for the HER at these materials and highlight a family of promising two-dimensional catalysts for water splitting.

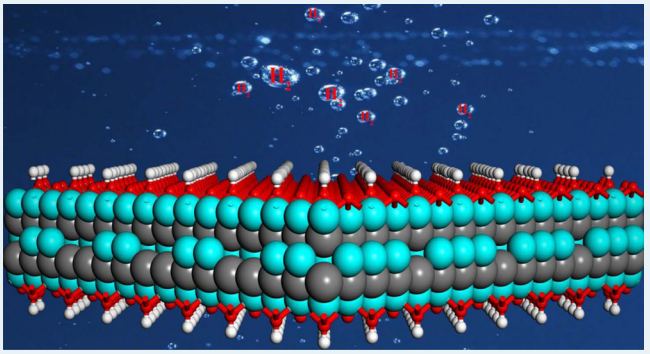

KEYWORDS: *water splitting, surface Pourbaix diagrams, termination, volcano curve, Gibbs free energy of hydrogen adsorption, functional groups*

INTRODUCTION

The production of hydrogen from water splitting offers an essential solution for today's environmental problems.[1,2] So far, the most efficient hydrogen evolution reaction (HER) catalysts are noble metals, such as platinum;[3] however, the scarcity of noble metals hampers their application as catalysts for large-scale hydrogen generation.[4] In recent years, some promising noble metal-free catalysts with high activity toward the HER have been extensively studied, including MoS_2,[5−7] metal phosphides,[8] g-C_3N_4,[9−11] and nanocarbon.[12] However, one significant drawback of these two-dimensional (2D) catalysts is that they are semiconducting with poor charge transfer performance.[5] Even though 1T-MoS_2 is conductive, it is unstable under ambient conditions.[7] Another drawback is that the catalytically active sites are confined to the edge or defective atoms, while the majority of the in-plane atoms are catalytically inert.[6,12,13] Therefore, the ongoing search for new stable 2D HER catalysts with excellent charge transfer kinetics and many catalytically active sites is of paramount significance.

2D MXenes, early transition metal (M) carbides and nitrides (X), have recently been exfoliated via selective etching of the "A" element in the counterpart MAX phases.[14] Here, M, A, and X represent an early transition metal, a main group IIIA or IVA element, and a carbon and/or nitrogen atom, respectively. The chemical formula of 2D MXenes is M_nX_{n-1} (n = 2−4), where the top and bottom layers consist of the transition metals that are exposed. Since the synthesis of the first MXene, i.e., Ti_3C_2, from the MAX (Ti_3AlC_2) phase in 2011,[15] this new family of 2D materials has attracted intense attention.[14,16,17] Although a variety of 2D MXenes have been theoretically predicted,[18] only a few of them, including Ti_2C,[19] V_2C,[20] Nb_2C,[21] Ti_3C_2,[15] and Nb_4C_3,[22] have been synthesized to date. Experimentally, the exposed M atoms in 2D MXenes are generally terminated by F*, OH*, and O* groups,[14,23] where the asterisk denotes one adsorption site on the surface. Significantly, the surface O-terminated 2D MXenes have demonstrated promise in applications in Li-ion batteries,[24,25] supercapacitors,[26,27] fuel cells,[28,29] hydrogen evolution,[30,31] CO oxidation,[32] and gas sensors[33] because of their excellent conductivity and tunable surface terminations.[34]

The purpose of this study is to explore (i) the stability of 2D MXenes with oxygen/hydroxyl (O*/OH*) termination[14,35] and (ii) whether the experimentally realized MXenes (Ti_2C, V_2C, Nb_2C, Ti_3C_2, and Nb_4C_3) with O* or OH* termination can act as efficient HER catalysts. First, we find that 2D MXenes commonly terminated with an O*/OH* group in the experiment are metallic. Then surface Pourbaix diagrams were constructed to identify the most stable surface structures of 2D

Received: September 26, 2016
Revised: November 23, 2016
Published: December 2, 2016

Downloaded via LAWRENCE BERKELEY NATL LABORATORY on June 4, 2020 at 05:36:07 (UTC).
See https://pubs.acs.org/sharingguidelines for options on how to legitimately share published articles.

© 2016 American Chemical Society

DOI: 10.1021/acscatal.6b02754
ACS Catal. 2017, 7, 494−500

MXenes under relevant potentials versus the standard hydrogen electrode (U_{SHE}) and pH values. Under standard conditions, Ti_2C, V_2C, and Ti_3C_2 are terminated by a mixture of OH* and O*, while Nb_2C and Nb_4C_3 are fully terminated by O*. The HER activity of oxygen-terminated MXenes is further evaluated by calculating the Gibbs free energy of the adsorption of atomic hydrogen ($\Delta G^0_{H^*}$). Remarkably, surface oxygen atoms are for the first time demonstrated to be active sites for the HER. In addition, the HER performances of MXences with and without oxygen termination are compared with a volcano curve. The results show that oxygen termination promotes hydrogen release and increases the exchange current dramatically.

COMPUTATIONAL DETAILS

All calculations were performed by using density functional theory (DFT) as implemented in the Vienna Ab-initio Simulation Package (VASP) code.[36,37] Blöchl's all-electron, frozen-core projector augmented wave (PAW) method[38] was used to represent nuclei and core electrons, and only the electrons in brackets of Ti[$3d^2 4s^2$], V[$3d^3 4s^2$], Nb[$4p^6 4d^4 5s^1$], O[$2s^2 2p^4$], and H[$1s^1$] are treated as valence electrons. The exchange-correlation interactions were described by the generalized gradient approximation[39] in the form of the Perdew–Burke–Ernzerhof functional.[40] The van der Waals interaction was described by using the empirical correction in Grimme's scheme, i.e., DFT+D_3, in all calculations.[41] The electron wave functions were expanded by plane waves with cutoff energies of 500 eV, and the convergence tolerance for the residual force and energy on each atom during structure relaxation were set to 0.005 eV/Å and 10^{-5} eV, respectively. The vacuum space in the z-direction was >20 Å, which was enough to prevent the interaction between periodical images. The Brillouin zone was sampled with the Monkhorst–Pack mesh with a K-point of $9 \times 9 \times 1$ for the unit cell and $5 \times 5 \times 1$ and $2 \times 2 \times 1$ for the supercell in reciprocal space during geometry optimization. Hybrid functional methods based on the Heyd–Scuseria–Ernzerhof (HSE06) method[42,43] were adopted to determine the accurate band structures. The standard hydrogen electrode (U_{SHE}) was theoretically defined in solution [pH 0, $p(H_2)$ = 1 bar].

Gibbs Free Energy of Hydrogen Adsorption. Under standard conditions, the overall HER pathway can be described by eq 1

$$H^+(aq) + e^- \rightarrow \frac{1}{2}H_2(g) \quad \Delta G^0 = 0\ \text{eV} \tag{1}$$

comprising an initial state $H^+(aq) + e^-$, an intermediate adsorbed H*, and the final product, $^1/_2H_2(g)$. The total energies of $H^+(aq) + e^-$ and $^1/_2H_2(g)$ are equal. Therefore, the Gibbs free energy of the adsorption of the intermediate hydrogen on a catalyst ($\Delta G^0_{H^*}$) is a key descriptor of the HER activity of the catalyst and is obtained by eq 2

$$\Delta G^0_{H^*} = \Delta E_H + \Delta E_{ZPE} - T\Delta S_H \tag{2}$$

where ΔE_{ZPE} and ΔS_H are the difference in zero-point energy and the entropy between atomic hydrogen adsorption and hydrogen in the gas phase, respectively. The contributions from the catalysts to both ΔE_{ZPE} and ΔS_H are small and neglected. Therefore, ΔE_{ZPE} is obtained by eq 3[44]

$$\Delta E_{ZPE} = E^{nH}_{ZPE} - E^{(n-1)H}_{ZPE} - \frac{1}{2}E^{H_2}_{ZPE} \tag{3}$$

where E^{nH}_{ZPE} is the zero-point energy of n adsorbed atomic hydrogens on the catalyst without the contribution of the catalyst. The vibration frequency of H* adsorption on $Ti_3C_2O_2$ with $^1/_8$ coverage (n = 1) is 3705.0 cm^{-1}, which is not sensitive to coverage. $E^{H_2}_{ZPE}$ is the zero-point energy of H_2 in the gas phase. The calculated frequency of H_2 gas is 4289.4 cm^{-1}. The ΔS_H is obtained by eq 4

$$\Delta S_H \cong -\frac{1}{2}S^0_{H_2} \tag{4}$$

and $S^0_{H_2}$ is the entropy of H_2 gas under the standard condition.[45] Therefore, eq 2 can be rewritten as eq 5:

$$\Delta G^0_{H^*} = \Delta E_H + 0.30\ \text{eV} \tag{5}$$

ΔE_H is the differential hydrogen adsorption energy, which is defined by eq 6:

$$\Delta E_H = E_{nH^*} - E_{(n-1)H^*} - \frac{1}{2}E_{H_2} \tag{6}$$

where the asterisk denotes the catalyst. E_{nH^*}, $E_{(n-1)H^*}$, and E_{H_2} represent total energies of the catalyst with n adsorbed hydrogen atoms, the catalyst with $n-1$ adsorbed atomic hydrogen atoms, and H_2 gas, respectively.

Surface Pourbaix Diagrams. The surface Pourbaix diagrams of all five MXenes were constructed by plotting the most stable surface state under the relevant U_{SHE} and pH. In our model, we assumed that the oxidation of water to OH* and O* on MXenes occurred through the following steps as suggested in ref 46:

$$H_2O + * \rightarrow OH^* + H^+ + e^- \tag{7}$$

$$OH^* \rightarrow O^* + H^+ + e^- \tag{8}$$

Under standard conditions, the free energy of $H^+ + e^-$ is equal to $^1/_2H_2$ as indicated in eq 1. Therefore, eqs 7 and 8 can be rewritten as eqs 9 and 10, respectively:

$$H_2O + * \rightarrow OH^* + \frac{1}{2}H_2 \quad \Delta G^0_9 \tag{9}$$

$$OH^* \rightarrow O^* + \frac{1}{2}H_2 \quad \Delta G^0_{10} \tag{10}$$

The Gibbs free energies of eq 9 (ΔG^0_9) and eq 10 (ΔG^0_{10}) are obtained by eq 11

$$\Delta G^0 = \Delta E + \Delta E_{ZPE} - T\Delta S \tag{11}$$

where ΔE is the energy difference from eq 9 or 10. The values for $E_{ZPE} - T\Delta S$ are calculated on the basis of values from Table 1 of ref 47.

Both eqs 7 and 8 are dependent on the pH and potential U through the chemical potential of H^+ and e^-, respectively, while eqs 9 and 10 are not. To include the effects of pH and potential U, eq 11 are rewritten as eqs 12 and 13:

$$\Delta G_9 = \Delta G^0_9 - eU_{SHE} - k_b T \ln 10 \times \text{pH} \tag{12}$$

$$\Delta G_{10} = \Delta G^0_{10} - eU_{SHE} - k_b T \ln 10 \times \text{pH} \tag{13}$$

The free energy change of OH* and O* termination can be expressed by eqs 14 and 15:

$$\Delta G_{OH^*} = \Delta G_9 \tag{14}$$

$$\Delta G_{OH^*} = \Delta G_9 + \Delta G_{10} \tag{15}$$

DOI: 10.1021/acscatal.6b02754
ACS Catal. 2017, 7, 494–500

On the basis of eqs 14 and 15, we can calculate the free energy of MXenes with different coverages of OH* and O* termination at different coverages and under different conditions. The free energies of MXenes with a mix of terminations $[M_nC_{n-1}(OH)_x(O)_y$, where $x + y \leq 2]$ are obtained by

$$\Delta G_{mix} = x\Delta G_{OH*} + y\Delta G_{O*} = (x + y)\Delta G_9 + y\Delta G_{10} = (x + y)\Delta G_9^0 + y\Delta G_{10}{}^0 - (x + 2y)(eU_{SHE} + k_bT \ln 10 \times pH) \quad (16)$$

The most stable state of the surface under the relevant conditions is used to construct the surface Pourbaix diagrams. A numerical example of Ti_2C can be found in Table S1.

Volcano Curve. In the volcano curve, the average Gibbs free energies of hydrogen adsorption (ΔG^a_{H*}) on bare MXenes with a hydrogen coverage of $\theta = 1$ and oxygen-terminated MXenes with a hydrogen coverage of $\theta = {}^1/_2$ are used to calculate the theoretical exchange current, i_0. To obtain ΔG^a_{H*}, only eq 6 was rewritten to

$$\Delta E^a_H = E_{nH*} - E_{cat} - \frac{n}{2}E_{H_2} \quad (17)$$

where E_{cat} is the total energy of the catalyst.

The exchange current is based on Norskov's assumption[48] (see the reference for details). If $\Delta G^a_{H*} \leq 0$, the following expression for the exchange current at pH 0 is used:

$$i_0 = -ek_0 \frac{1}{1 + \exp(-\Delta G^a_{H*}/k_bT)} \quad (18)$$

For another case ($\Delta G^a_{H*} > 0$), the exchange current is calculated by

$$i_0 = -ek_0 \frac{1}{1 + \exp(\Delta G^a_{H*}/k_bT)} \quad (19)$$

where k_0 is the rate constant. As there are no experimental data available, k_0 is set to 1.

RESULTS AND DISCUSSION

Excellent Electrical Conductivity. The structural models of MXenes (M_nC_{n-1}), oxygen-terminated MXenes ($M_nC_{n-1}O_2$), and hydroxyl-terminated MXenes $[M_nC_{n-1}(OH)_2]$ are presented in Figure 1. The 2D MXenes investigated in this work are 2D Ti_2C, V_2C, Nb_2C, Ti_3C_2, and Nb_4C_3, which have all been realized experimentally.[15,19−22] As shown in panels a, d, and g of Figure 1, the bare MXenes are packed in the face-centered cubic arrangement with two exposed metal layers, displaying $P3m1$ symmetry. The calculated band structures of bare MXenes are presented in Figure 2a−e, clearly indicating that all the MXenes are metallic. Because the exposed metal atoms are electron donors, they are vulnerable to electronegative functional groups, such as an OH* and O* group, during their experimental synthesis.

The surfaces of MXenes that are fully terminated by O* (Figure 1b,e,h) or OH* (Figure 1c,f,i) are also constructed. The most stable adsorption sites for O*/OH* functional groups are first examined, and we find the hollow sites that are pointed toward the second layer of metal atoms (face-centered cubic hollow sites) on both sides of MXenes are the most energy-favorable sites for the adsorption of O*/OH* functional groups. As Ti_2C is terminated by O* (Ti_2CO_2), the Ti atoms are in their most oxidized state (+4), achieved by donating their

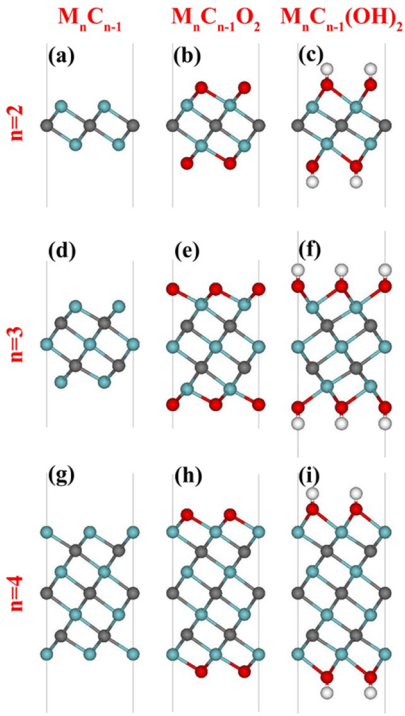

Figure 1. Models of MXenes (M_nC_{n-1}), oxygen-terminated MXenes ($M_nC_{n-1}O_2$), and hydroxyl-terminated MXenes $[M_nC_{n-1}(OH)_2]$. n varies from 2 to 4. Color code: metal, cyan; carbon, gray; oxygen, red; hydrogen, white.

electrons to the negatively charged oxygen and carbon atoms (−2 and −4, respectively).[35] Therefore, the Fermi level shift below the d band (conductive band) resulted in Ti_2CO_2 being semiconducting with a gap of 0.78 eV (seen in Figure 2f). Interestingly, once one hydrogen atom is adsorbed by Ti_2CO_2, the band gap is closed and Ti_2CO_2 becomes metallic (see Figure S1). This is mainly attributed to some spare electrons in the d band of Ti atoms after donation of an electron partially to the negatively charged OH^- (−1). Except for Ti_2C, all other 2D MXenes terminated with functional groups are metallic. Therefore, O*- or OH*-terminated 2D MXenes can display excellent charge transfer performance for efficient HER.

High Thermal Stability. In the following, the surface Pourbaix diagrams of all five 2D MXenes are constructed by plotting the thermodynamically most stable surface state under the relevant U_{SHE} and pH values (see Figure 3).[21] As mentioned above, the bare MXenes are very vulnerable to electron-accepting functional groups such as OH* and O*. In an acidic solution (pH 0), negative U_{SHE} values (reducing environment) as low as −2.63, −1.91, −2.04, −2.53, and −1.51 V are required to protect Ti_2C, V_2C, Nb_2C, Ti_3C_2, and Nb_4C_3, respectively, from oxidation by H_2O. A more negative potential is necessary to protect the bare MXenes at high pH values with a slope of −0.059 V/pH. When the potential is above the cathodic protection potential of the 2D MXenes, water starts to oxidize and the MXenes are covered by ${}^1/_8$ ML OH*. As the potential increases, more OH* adsorbs on the 2D MXenes, and the level finally reaches 1 ML OH* $[M_nX_{n-1}(OH)_2]$. For instance, 2D Ti_2C is fully terminated by OH* at a U_{SHE} of −0.34 V. The hydroxyl is partially oxidized if the potential continues to increase, and finally, the MXenes are terminated by a mixture of O* and OH*. At higher potentials, all the hydroxyls on MXenes will be oxidized, and the most stable O*-

DOI: 10.1021/acscatal.6b02754
ACS Catal. 2017, 7, 494−500

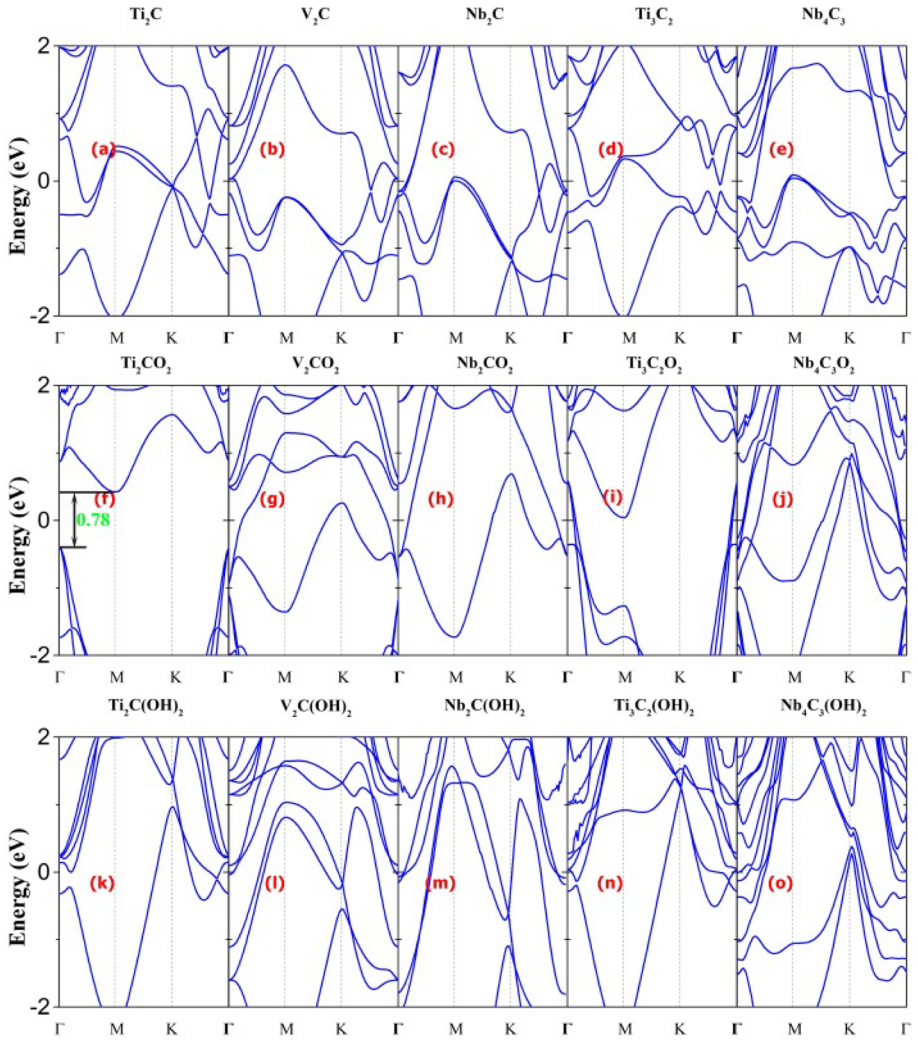

Figure 2. Band structure of MXenes [M_nC_{n-1} (a–e)], oxygen-terminated MXenes [$M_nC_{n-1}O_2$ (f–j)], and hydroxyl-terminated MXenes [$M_nC_{n-1}(OH)_2$ (k–o)]. The Femi level is set to zero.

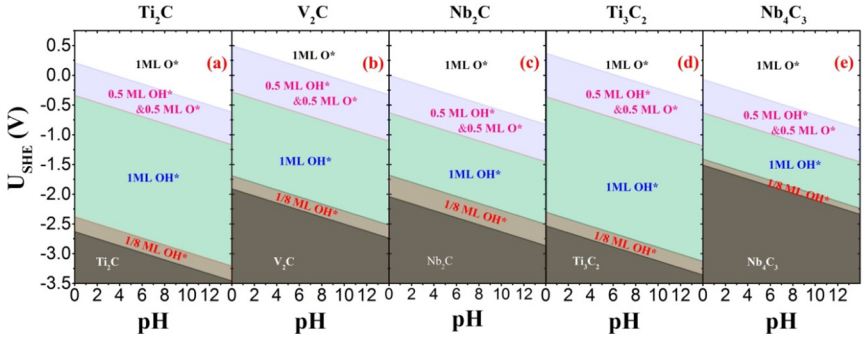

Figure 3. Surface Pourbaix diagrams of Ti_2C, V_2C, Nb_2C, Ti_3C_2, and Nb_4C_3. The most thermodynamically stable states of the surface under relevant U_{SHE} conditions and pH values are labeled by the terminations.

terminated MXenes [$M_nX_{n-1}(O)_2$] will be formed. The lowest U_{SHE} values for 2D MXenes with full O* termination are 0.21 V (Ti_2C), 0.50 V (V_2C), 0.00 V (Nb_2C), 0.37 V (T_3C_2), and −0.07 V (Nb_4C_3) in an acidic solution (pH 0). Therefore, under standard conditions, Ti_2C, V_2C, and Ti_3C_2 are terminated by a mixture of OH* and O* while Nb_2C and Nb_4C_3 are fully terminated by O*.

The 2D MXenes must exhibit high stability and excellent HER activity at a U_{SHE} of 0 V if they are to be used as efficient HER catalysts. Herein, we investigated the relative stability of MXenes with different terminations as a function of pH at a U_{SHE} of 0 V (see Figure 4). The bottom line corresponds to the states with the lowest free energy, i.e., the most stable state at a given pH. The O*/OH*-terminated MXenes are much more stable than bare 2D MXenes or partially terminated MXenes ($^1/_8$ ML OH*). In an acidic solution (pH 0), the most stable states of Nb_2C and Nb_3C_2 are O*-terminated surfaces while Ti_2C, V_2C, and Ti_3C_2 terminated by a mixture of O* and OH*

DOI: 10.1021/acscatal.6b02754
ACS Catal. 2017, 7, 494–500

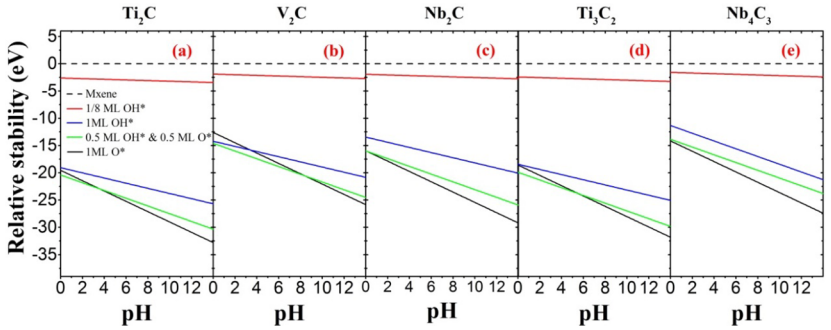

Figure 4. Stability of O* and OH* on Ti_2C, V_2C, Nb_2C, Ti_3C_2, and Nb_4C_3 at a U_{SHE} of 0 V. The line labels of panels a–e are the same and are shown in panel a only.

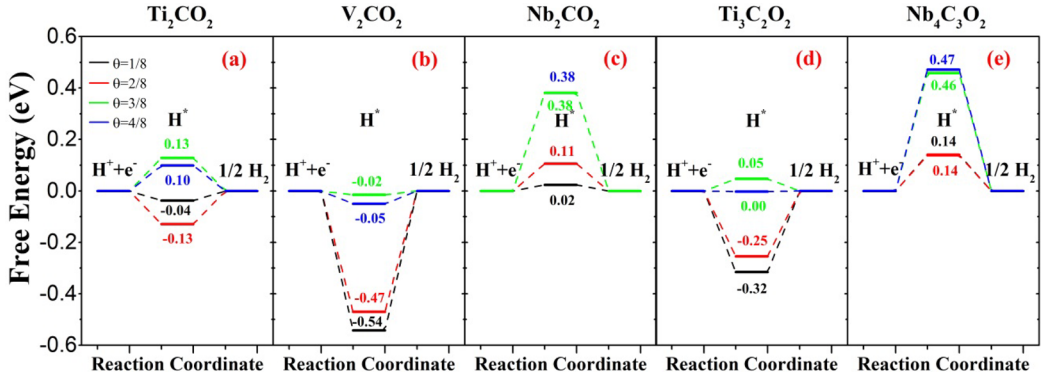

Figure 5. Free energy diagram of HER processing on Ti_2CO_2, V_2CO_2, Nb_2CO_2, $Ti_3C_2O_2$, and $Nb_4C_3O_2$ under standard conditions. The line labels (a–e) are the same and shown in only panel a.

are the most energetically favorable. As the pH value is increased, the hydrogen atom in the hydroxyl group on the 2D MXenes (Ti_2C, V_2C, and Ti_3C_2) can be dissociated. When the pH values are above 3.6, 8.4, and 5.5 for Ti_2C, V_2C, and Ti_3C_2, respectively (the black lines cross the green lines in Figure 4a,b,d), these MXenes are fully terminated by O*. Collectively, these findings are consistent with the experimental observation that MXenes terminated by a mixture of OH* and O* are highly stable,[14,23] and thus, it is reasonable to investigate MXenes terminated by a mixture of OH* and O* as the most appropriate catalysts for the HER.

Hydrogen Evolution Reaction Activity. In the following, the HER activity of O*-terminated MXenes ($M_nC_{n-1}O_2$) under standard conditions is investigated. The Gibbs free energies for the adsorption of atomic hydrogen ($\Delta G^0_{H^*}$) on $M_nC_{n-1}O_2$ at different coverages have been calculated as shown in Figure 5. The $\Delta G^0_{H^*}$ of an ideal catalyst for the HER should be close to 0 ($\Delta G^0_{H^*} \rightarrow 0$). It is worth noting that there are two surface O* layers in $M_nC_{n-1}O_2$ that function as the active sites for the HER. In a $2 \times 2 \times 1$ $M_nC_{n-1}O_2$ supercell, there are eight O* atoms and different H coverages can be simulated with an increment of $^1/_8$.

For Ti_2CO_2 with a hydrogen coverage of $^1/_8$, $\Delta G^0_{H^*}$ is −0.04 eV, which is nearly perfect for the HER. When the coverage is increased to $^2/_8$, the interaction between H* and the oxygen atoms is slightly enhanced, with a $\Delta G^0_{H^*}$ of −0.13 eV. As the coverage continues to increase, the interaction between H* and the oxygen atoms is slightly weakened with $\Delta G^0_{H^*}$ values of 0.13 and 0.10 eV for H coverages of $^3/_8$ and $^4/_8$, respectively. When an even number of hydrogen atoms is adsorbed in a $2 \times 2 \times 1$ Ti_2CO_2 supercell, the system can be stabilized by H* binding due to higher symmetry. Therefore, the hydrogen binding free energy at H coverages of $^2/_8$ ($^4/_8$) is lower than that at H coverages of $^1/_8$ ($^3/_8$). The $\Delta G^0_{H^*}$ for hydrogen coverage ranging from $^1/_{18}$ to $^4/_{18}$ ($|\Delta G^0_{H^*}| < 0.15$) is close to 0, indicating that Ti_2CO_2 is potentially an excellent catalyst for the HER over a wide range of H coverages.

In the case of V_2CO_2 and $Ti_3C_2O_2$ at lower coverages ($^1/_8$ and $^2/_8$), the interactions between H* and the oxygen atoms are too strong as evidenced by a relatively large negative $\Delta G^0_{H^*}$ value, which will prevent the further release of hydrogen from the catalyst surface. When the H coverages are increased to $^3/_8$ and $^4/_8$, $\Delta G^0_{H^*}$ is very close to 0 as shown in panels b and d of Figure 5. In contrast, Nb_2CO_2 and $Nb_4C_3O_2$ (see panels c and e, respectively, of Figure 5) show HER activity at only relatively low H coverages ($^1/_8$ and $^2/_8$), while the interaction between H* and oxygen atoms of Nb_2CO_2 and $Nb_4C_3O_2$ at higher coverages is too weak for hydrogen to bind to the catalyst.

To compare the HER performance of 2D MXenes with or without oxygen termination, a volcano curve is plotted as shown in Figure 6. The average Gibbs free energies of hydrogen adsorption ($\Delta G^a_{H^*}$) on bare 2D MXenes with a hydrogen coverage of $\theta = 1$ (see Table S2) and oxygen-terminated MXenes with a hydrogen coverage of $\theta = ^1/_2$ (see Table S3) are calculated to obtain the theoretical exchange current, i_0. The MXenes' HER performance can be quantitatively evaluated by the position of its i_0 and $\Delta G^a_{H^*}$ values relative to the volcano peak (the closer the position of these values to the peak, the better the catalyst).[48] Catalysts with negative and positive $\Delta G^a_{H^*}$ values are located around the left and right legs of the volcano, respectively, while catalysts with $\Delta G^a_{H^*}$ values close to zero are located at the peak of the volcano curve. Clearly, the interactions of H* and bare MXenes are too strong with a very large negative $\Delta G^a_{H^*}$ of less than

DOI: 10.1021/acscatal.6b02754
ACS Catal. 2017, 7, 494–500

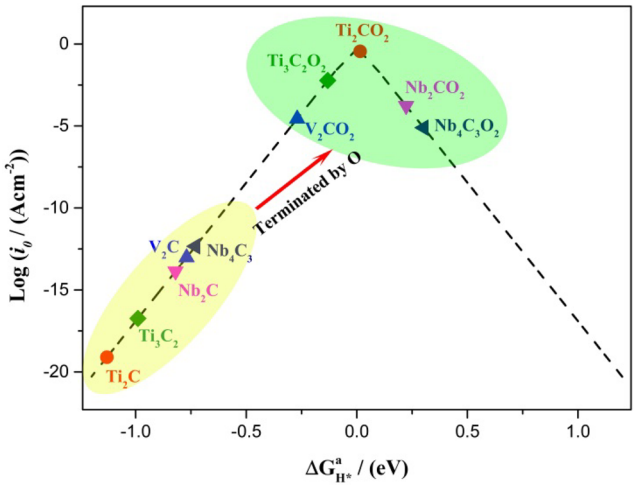

Figure 6. Volcano curve of exchange current (i_0) as a function of the average Gibbs free energy of hydrogen adsorption ($\Delta G^a_{H^*}$).

−0.73 eV (see Table S2). The very large negative $\Delta G^a_{H^*}$ on bare MXenes is located at the bottom of the left leg with a very low exchange current. The negative $\Delta G^a_{H^*}$ can be further optimized by oxygen termination. With oxygen termination, the interaction of H* and the MXenes is much weaker with a $\Delta G^a_{H^*}$ around 0 (see Table S3). The weak interaction promotes hydrogen release and results in a very high exchange current, which is favorable for the HER. It is worth noting that the $\Delta G^a_{H^*}$ of Ti_2CO_2 is only 0.01 eV and the i_0 is located at the peak of the volcano curve. Therefore, the Ti_2CO_2 is expected to display the best HER performance, followed by $Ti_3C_2O_2$ and Nb_2CO_2, based on our results.

To fully understand the process of HER on the MXenes, the two generally accepted HER mechanisms, Volmer−Heyrovsky and Volmer−Tafel reactions,[49] were studied as shown in Figure S2. The difference in these two pathways is the second step: $H^+ + e^- + H^* \rightarrow H_2$ (Heyrovsky) and $H^* + H^* \rightarrow H_2$ (Tafel). Herein, we compare the activation barrier during the HER that follows the Heyrovsky pathway and Tafel pathway on a 3 × 3 × 1 Ti_2CO_2 supercell with one surface covered by H*. Eight H_2O molecules are used to simulate the solution effects following the model used in refs 50 and 51. As we can see, the barrier for the Heyrovsky step (0.29 eV) is much smaller than that for the Tafel step (0.99 eV). Therefore, the HER follows the Heyrovsky mechanism on oxygen-terminated MXenes.

CONCLUSIONS

In summary, we have demonstrated that 2D MXenes commonly terminated with a mixture of O* and OH* in experiments exhibit excellent HER performance. Under standard conditions, the surface Pourbaix diagrams clearly indicate that O*/OH*-terminated MXenes are the most stable states, and all of them are metallic, thus favoring excellent charge transfer. The surface oxygen atoms on the top and bottom layers of 2D MXenes function as the catalytic active sites for the HER with a suitable interaction strength between H* and 2D MXenes. If they are coupled with a suitable semiconductor, metallic 2D MXenes under standard conditions could be an efficient cocatalyst for the photocatalytic HER. Our findings demonstrate that O terminations act as catalytic active sites for efficient HER and highlight a new family of promising noble metal-free HER catalysts for future experimental verification.

ASSOCIATED CONTENT

Supporting Information

The Supporting Information is available free of charge on the ACS Publications website at DOI: 10.1021/acscatal.6b02754.

DOS of different numbers of hydrogens adsorbed on a 2 × 2 × 1 Ti_2CO_2 supercell, numerical example of Ti_2C, $\Delta G^a_{H^*}$ on bare MXenes at a H* coverage of 1 and oxygen-terminated MXenes at a H* coverage of $^1/_2$, optimized geometry of oxygen-terminated MXenes, and the HER mechanism (PDF)

AUTHOR INFORMATION

Corresponding Author

*E-mail: aijun.du@qut.edu.au. Phone: +61 731386980.

ORCID

Anthony P. O'Mullane: 0000-0001-9294-5180

Aijun Du: 0000-0002-0369-3283

Notes

The authors declare no competing financial interest.

ACKNOWLEDGMENTS

We acknowledge generous grants of high-performance computer time from the computing facility at QUT and Australian National Facility. A.D. greatly appreciates the ARC QEII Fellowship (DP110101239) and financial support from ARC via the Discovery Project (DP130102420).

REFERENCES

(1) Ahmad, H.; Kamarudin, S. K.; Minggu, L. J.; Kassim, M. *Renewable Sustainable Energy Rev.* **2015**, *43*, 599−610.
(2) Maeda, K. *J. Photochem. Photobiol., C* **2011**, *12* (4), 237−268.
(3) Subbaraman, R.; Tripkovic, D.; Strmcnik, D.; Chang, K.-C.; Uchimura, M.; Paulikas, A. P.; Stamenkovic, V.; Markovic, N. M. *Science* **2011**, *334* (6060), 1256−1260.
(4) Jiao, Y.; Zheng, Y.; Jaroniec, M.; Qiao, S. Z. *Chem. Soc. Rev.* **2015**, *44* (8), 2060−2086.
(5) Lukowski, M. A.; Daniel, A. S.; Meng, F.; Forticaux, A.; Li, L.; Jin, S. *J. Am. Chem. Soc.* **2013**, *135* (28), 10274−10277.
(6) Jaramillo, T. F.; Jørgensen, K. P.; Bonde, J.; Nielsen, J. H.; Horch, S.; Chorkendorff, I. *Science* **2007**, *317* (5834), 100−102.
(7) Gao, G.; Jiao, Y.; Ma, F.; Jiao, Y.; Waclawik, E.; Du, A. *J. Phys. Chem. C* **2015**, *119* (23), 13124−13128.
(8) Kibsgaard, J.; Tsai, C.; Chan, K.; Benck, J. D.; Norskov, J. K.; Abild-Pedersen, F.; Jaramillo, T. F. *Energy Environ. Sci.* **2015**, *8* (10), 3022−3029.
(9) Zheng, Y.; Jiao, Y.; Chen, J.; Liu, J.; Liang, J.; Du, A.; Zhang, W.; Zhu, Z.; Smith, S. C.; Jaroniec, M.; Lu, G. Q.; Qiao, S. Z. *J. Am. Chem. Soc.* **2011**, *133* (50), 20116−20119.
(10) Gao, G.; Jiao, Y.; Ma, F.; Jiao, Y.; Waclawik, E.; Du, A. *J. Catal.* **2015**, *332*, 149−155.
(11) Gao, G.; Jiao, Y.; Ma, F.; Jiao, Y.; Waclawik, E.; Du, A. *Phys. Chem. Chem. Phys.* **2015**, *17* (46), 31140−31144.
(12) Fei, H.; Dong, J.; Arellano-Jiménez, M. J.; Ye, G.; Dong Kim, N.; Samuel, E. L.; Peng, Z.; Zhu, Z.; Qin, F.; Bao, J.; Yacaman, M. J.; Ajayan, P. M.; Chen, D.; Tour, J. M. *Nat. Commun.* **2015**, *6*, 8668.
(13) Gao, G.; Sun, Q.; Du, A. *J. Phys. Chem. C* **2016**, *120* (30), 16761−16766.
(14) Naguib, M.; Mochalin, V. N.; Barsoum, M. W.; Gogotsi, Y. *Adv. Mater.* **2014**, *26* (7), 992−1005.
(15) Naguib, M.; Kurtoglu, M.; Presser, V.; Lu, J.; Niu, J.; Heon, M.; Hultman, L.; Gogotsi, Y.; Barsoum, M. W. *Adv. Mater.* **2011**, *23* (37), 4248−4253.
(16) Azofra, L. M.; Li, N.; MacFarlane, D. R.; Sun, C. *Energy Environ. Sci.* **2016**, *9* (8), 2545−2549.

DOI: 10.1021/acscatal.6b02754
ACS Catal. 2017, 7, 494−500

(17) Lei, J.-C.; Zhang, X.; Zhou, Z. *Front. Phys.* **2015**, *10*, 276−286.
(18) Tang, Q.; Zhou, Z.; Chen, Z. *WIRs Comput. Mol. Sci.* **2015**, *5* (5), 360−379.
(19) Naguib, M.; Mashtalir, O.; Carle, J.; Presser, V.; Lu, J.; Hultman, L.; Gogotsi, Y.; Barsoum, M. W. *ACS Nano* **2012**, *6* (2), 1322−1331.
(20) Dall'Agnese, Y.; Taberna, P.-L.; Gogotsi, Y.; Simon, P. *J. Phys. Chem. Lett.* **2015**, *6* (12), 2305−2309.
(21) Naguib, M.; Halim, J.; Lu, J.; Cook, K. M.; Hultman, L.; Gogotsi, Y.; Barsoum, M. W. *J. Am. Chem. Soc.* **2013**, *135* (43), 15966−15969.
(22) Ghidiu, M.; Naguib, M.; Shi, C.; Mashtalir, O.; Pan, L. M.; Zhang, B.; Yang, J.; Gogotsi, Y.; Billinge, S. J. L.; Barsoum, M. W. *Chem. Commun.* **2014**, *50* (67), 9517−9520.
(23) Mashtalir, O.; Naguib, M.; Mochalin, V. N.; Dall'Agnese, Y.; Heon, M.; Barsoum, M. W.; Gogotsi, Y. *Nat. Commun.* **2013**, *4*, 1716.
(24) Sun, D.; Wang, M.; Li, Z.; Fan, G.; Fan, L.-Z.; Zhou, A. *Electrochem. Commun.* **2014**, *47*, 80−83.
(25) Liang, X.; Garsuch, A.; Nazar, L. F. *Angew. Chem.* **2015**, *127* (13), 3979−3983.
(26) Lukatskaya, M. R.; Mashtalir, O.; Ren, C. E.; Dall'Agnese, Y.; Rozier, P.; Taberna, P. L.; Naguib, M.; Simon, P.; Barsoum, M. W.; Gogotsi, Y. *Science* **2013**, *341* (6153), 1502−1505.
(27) Ling, Z.; Ren, C. E.; Zhao, M.-Q.; Yang, J.; Giammarco, J. M.; Qiu, J.; Barsoum, M. W.; Gogotsi, Y. *Proc. Natl. Acad. Sci. U. S. A.* **2014**, *111* (47), 16676−16681.
(28) Xie, X.; Chen, S.; Ding, W.; Nie, Y.; Wei, Z. *Chem. Commun.* **2013**, *49* (86), 10112−10114.
(29) Ma, T. Y.; Cao, J. L.; Jaroniec, M.; Qiao, S. Z. *Angew. Chem., Int. Ed.* **2016**, *55* (3), 1138−1142.
(30) Ling, C.; Shi, L.; Ouyang, Y.; Chen, Q.; Wang, J. *Adv. Sci.* **2016**, *3*, 1600180−1600186.
(31) Seh, Z. W.; Fredrickson, K. D.; Anasori, B.; Kibsgaard, J.; Strickler, A. L.; Lukatskaya, M. R.; Gogotsi, Y.; Jaramillo, T. F.; Vojvodic, A. *ACS Energy Lett.* **2016**, *1* (3), 589−594.
(32) Zhang, X.; Lei, J.; Wu, D.; Zhao, X.; Jing, Y.; Zhou, Z. *J. Mater. Chem. A* **2016**, *4* (13), 4871−4876.
(33) Yu, X.-f.; Li, Y.-c.; Cheng, J.-b.; Liu, Z.-b.; Li, Q.-z.; Li, W.-z.; Yang, X.; Xiao, B. *ACS Appl. Mater. Interfaces* **2015**, *7* (24), 13707−13713.
(34) Zhang, X.; Zhao, X.; Wu, D.; Jing, Y.; Zhou, Z. *Nanoscale* **2015**, *7* (38), 16020−16025.
(35) Khazaei, M.; Arai, M.; Sasaki, T.; Chung, C.-Y.; Venkataramanan, N. S.; Estili, M.; Sakka, Y.; Kawazoe, Y. *Adv. Funct. Mater.* **2013**, *23* (17), 2185−2192.
(36) Kresse, G.; Furthmüller, J. *Comput. Mater. Sci.* **1996**, *6* (1), 15−50.
(37) Kresse, G.; Furthmüller, J. *Phys. Rev. B: Condens. Matter Mater. Phys.* **1996**, *54* (16), 11169−11186.
(38) Blöchl, P. E. *Phys. Rev. B: Condens. Matter Mater. Phys.* **1994**, *50* (24), 17953−17979.
(39) Perdew, J. P.; Burke, K.; Ernzerhof, M. *Phys. Rev. Lett.* **1996**, *77* (18), 3865−3868.
(40) Perdew, J. P.; Ernzerhof, M.; Burke, K. *J. Chem. Phys.* **1996**, *105* (22), 9982−9985.
(41) Grimme, S. *J. Comput. Chem.* **2006**, *27* (15), 1787−1799.
(42) Heyd, J.; Scuseria, G. E.; Ernzerhof, M. *J. Chem. Phys.* **2003**, *118* (18), 8207−8215.
(43) Heyd, J.; Scuseria, G. E.; Ernzerhof, M. *J. Chem. Phys.* **2006**, *124* (21), 219906.
(44) Tsai, C.; Abild-Pedersen, F.; Nørskov, J. K. *Nano Lett.* **2014**, *14* (3), 1381−1387.
(45) Atkins, P. *Physical Chemistry*, 10th ed.; Oxford University Press: Oxford, U.K., 2014.
(46) Hansen, H. A.; Rossmeisl, J.; Norskov, J. K. *Phys. Chem. Chem. Phys.* **2008**, *10* (25), 3722−3730.
(47) Valdés, Á.; Qu, Z. W.; Kroes, G. J.; Rossmeisl, J.; Nørskov, J. K. *J. Phys. Chem. C* **2008**, *112* (26), 9872−9879.
(48) Nørskov, J. K.; Bligaard, T.; Logadottir, A.; Kitchin, J.; Chen, J. G.; Pandelov, S.; Stimming, U. *J. Electrochem. Soc.* **2005**, *152* (3), J23−J26.
(49) Conway, B. E.; Tilak, B. V. *Electrochim. Acta* **2002**, *47* (22−23), 3571−3594.
(50) Skulason, E.; Karlberg, G. S.; Rossmeisl, J.; Bligaard, T.; Greeley, J.; Jonsson, H.; Norskov, J. K. *Phys. Chem. Chem. Phys.* **2007**, *9* (25), 3241−3250.
(51) Tang, Q.; Jiang, D.-e. *ACS Catal.* **2016**, *6* (8), 4953−4961.

DOI: 10.1021/acscatal.6b02754
ACS Catal. 2017, 7, 494−500